Monthly Notices of the ROYAL ASTRONOMICAL SOCIETY

MNRAS **535,** 2436–2448 (2024) https://doi.org/10.1093/mnras/stae2444
Advance Access publication 2024 October 26

Dynamics and structure of network magnetic fields: supergranular vortex expansion–contraction

Abraham C.-L. Chian,[1,2]★ Erico L. Rempel,[2,3] Luis Bellot Rubio[4] and Milan Gošić[5,6]

[1] *School of Computer and Mathematical Sciences, Adelaide University, Adelaide, SA 5005, Australia*
[2] *National Institute for Space Research (INPE), P.O. Box 515, São José dos Campos, São Paulo 12227-010, Brazil*
[3] *Aeronautics Institute of Technology (ITA), São José dos Campos, São Paulo 12228-900, Brazil*
[4] *Instituto de Astrofísica de Andalucía (IAA-CSIC), Apartado de Correos 3004, E-18080 Granada, Spain*
[5] *Lockheed Martin Solar and Astrophysics Laboratory, Palo Alto, CA 94304, USA*
[6] *Bay Area Environmental Research Institute, Moffett Field, CA 94035, USA*

Accepted 2024 October 23. Received 2024 September 9; in original form 2024 June 24

ABSTRACT

We report on the formation of a large magnetic coherent structure in a vortex expansion–contraction interval, resulting from the merger of two plasmoids driven by a supergranular vortex observed by *Hinode* in the quiet-Sun. Strong vortical flows at the interior of vortex boundary are detected by the localized regions of high values of the instantaneous vorticity deviation, and intense current sheets in the merging plasmoids are detected by the localized regions of high values of the local current deviation. The spatiotemporal evolution of the line-of-sight magnetic field, the horizontal electric current density, and the horizontal electromagnetic energy flux is investigated by elucidating the relation between velocity and magnetic fields in the photospheric plasma turbulence. A local and continuous amplification of magnetic field from 286 G to 591 G is detected at the centre of one merging plasmoid during the vortex expansion–contraction interval of 60 min. During the period of vortex contraction of 22.5 min, the line-of-sight magnetic field at the centre of plasmoid-1 (2) exhibits a steady decrease (increase), respectively, indicating a steady transfer of magnetic flux from plasmoid-1 to plasmoid-2. At the end of the vortex expansion–contraction interval, the two merging plasmoids reach an equipartition of electromagnetic energy flux, leading to the formation of an elongated magnetic coherent structure encircled by a shell of intense current sheets. Evidence of the disruption of a thin current sheet at the turbulent interface boundary layers of two merging plasmoids is presented.

Key words: Magnetic reconnection – Sun: granulation – Sun: magnetic fields – Sun: photosphere.

1 INTRODUCTION

Supergranulations are dynamical convection cells in the outer third of the solar radius distributed over the full solar surface with a characteristic horizontal scale of 30–35 Mm and a lifetime of 24–48 h, which were first revealed by Leighton, Noyes & Simon (1962) through Doppler measurements of solar surface flows. A comparative study by Simon & Leighton (1964) of magnetograms, spectroheliograms, and Dopplergrams established a strong spatial correlation between supergranular junctions and the network of concentration of strong magnetic flux in the quiet and active Sun. Thus, network (NE) magnetic fields are intense magnetic webs covering the entire surface of the Sun that are co-spatial with the boundaries of supergranular cells. The total flux contained by network magnetic fields is estimated to be of the order of 10^{23}–10^{24} Mx over the entire solar surface (Simon, Title & Weiss 2001; Hagenaar, Schrijver & Title 2003; Hagenaar, DeRosa & Schrijver 2008; Zhou, Wang & Jin 2013). This is comparable to the total flux brought to the solar surface by active regions at solar maximum ($\sim 8\times10^{23}$ Mx; Schrijver & Harvey 1994).

The network collects and disperses along the lanes between supergranules. Leighton (1964) interpreted the dispersal and migration of unipolar and bipolar magnetic regions on the Sun as a random-walk, diffusion-like process caused by supergranular convection flows in the Sun's outer layers. Active regions are centres of solar magnetic activity. The decay process of active regions spreads the previously concentrated magnetic flux over an ever-increasing area due to supergranular buffeting, forming large bipolar regions that slowly become part of the background field (van Driel-Gesztelyi & Green 2015). Hence, network magnetic fields are postulated to be the remnants of the magnetic fields of decaying active regions that have been modified by interactions with other network magnetic fields, with the internetwork magnetic fields, and with new active regions. Although network magnetic fields may evolve from active region magnetic fields, in general they are identified as small patches of fields of single polarity because they no longer retain a close connection to the original opposite polarity components. Note, however, in addition to active regions, other sources of network magnetic fields have been identified. Harvey & Martin (1973) discovered bipolar features (called ephemeral regions) with fluxes in the range of $5 - 30 \times 10^{18}$ Mx and lifetimes of several hours (Harvey, Harvey & Martin 1975; Title 2000; Chae et al. 2001; Hagenaar 2001; Hagenaar et al. 2003, 2008). They can be considered as the largest

★ E-mail: abraham.chian@gmail.com

and strongest internetwork (IN) features, comparable to individual NE patches. Martin (1990) suggested that 90 per cent of the network flux originates from ephemeral regions, while the weaker IN elements contribute only 10 per cent of the network flux. This hypothesis was challenged by Gošić et al. (2014) who showed that internetwork fields supply as much flux as is present in the network in only 9–13 h and can fully replace the entire network flux in about 18–24 h.

Recent advances in the study of Lagrangian and Eulerian coherent structures have significantly improved our understanding of the dynamics and structures of fluid and plasma turbulence (see reviews by Haller 2015 and Rempel et al. 2023). Even though the network and internetwork magnetic elements undergo emergence, merging or splitting, and network magnetic fields can diffuse either by flux dispersal or cancellation with nearby elements (Requerey et al. 2018), we have shown in a series of papers (Chian et al. 2014, 2019, 2020, 2023; Silva et al. 2018) that short- and long-term changes in photospheric turbulence in the quiet and active Sun are governed by elliptic and hyperbolic Lagrangian/Eulerian coherent structures. Our studies have demonstrated that vortices, which are elliptic Lagrangian/Eulerian coherent structures, play a fundamental role in changes of photospheric magnetic fields (Chian et al. 2014, 2019, 2023); furthermore, hyperbolic Lagrangian coherent structures corresponding to unstable/stable manifolds play a crucial role in the diffusion of network/internetwork magnetic elements. In this paper, we will present observational evidence that a long-duration vortex resulting from strong downdraft and shear located in vertices between supergranules is responsible for trapping/untrapping of magnetic flux and the formation of a magnetic coherent structure. The photospheric turbulence is permeated by a multitude of plasmoids associated with the footpoints of open and closed magnetic flux tubes (loops), which can be detected as magnetic vortex tubes using the technique of Lagrangian coherent structures (Rempel et al. 2017, 2019). The approach of Lagrangian/Eulerian coherent structures can be useful for studying solar magnetic diffusion and random walks, as well as flux emergence, dispersal, and cancellation.

The merger of plasmoids (magnetic flux tubes/ropes) plays a key role in charged particle acceleration, plasma heating, and generation of outflows (e.g. winds, jets, coronal mass ejections) in space and astrophysical plasma turbulence. For example, Gold & Hoyle (1960) proposed a solar flare model based on the merger of two coronal magnetic flux ropes whose footpoints are rooted in the photosphere. Recently, there is a growing interest in probing complex physical processes taking place at the footpoints of chromospheric/coronal magnetic flux ropes located at supergranular junctions, in both quiet and active regions of solar activities. Hence, it is important to address the question of how vortical flows in the photospheric supergranular turbulence drive the twisting/untwisting of magnetic field lines inside chromospheric/coronal loops that lead to their eruptions in solar microflares in the quiet Sun and solar flares in active regions.

Tu et al. (2005) made use of *SUMER (Solar Ultraviolet Measurements of Emitted Radiation)* and *MDI ((Michelson Doppler Imager)* data onboard *SOHO (Solar and Heliospheric Observatory)* to present evidence of solar wind originating from the funnels rooted near supergranulation boundaries in the network lanes of coronal holes. The study carried out by Innes et al. (2009) of quiet-Sun EUV images taken by *STEREO (Solar TErrestrial RElations Observatory)* showed that solar eruptions with characteristics of small coronal mass ejections (mini-CMEs) occur at the junctions of supergranular cells. By tracking the photospheric flows and magnetic fields, they found vortex-like structures at the supergranular junction preceding the eruptions. Yang et al. (2015) used *SDO* data to show that in the negative footpoint region of an inverse *J*-shaped dextral filament in the quiet Sun, a rotating network magnetic structure was formed by vortical flows and the convergence of several magnetic flux patches of the same polarity to supergranular junctions, which evolves into an EUV cyclone after 11 h. They showed that the EUV cyclone vanishes when the rotational motion of the rotating network magnetic structure ceases. Based on the observations of *Parker Solar Probe*, Bale et al. (2021) proposed that switchbacks are generated by interchange magnetic reconnection between closed and open magnetic flux ropes whose footpoints are anchored at supergranular junctions; moreover, Fargette et al. (2021) proposed that switchbacks are modulated by the solar surface convection patterns of supergranulations and granulations.

Wang et al. (2014) showed that the two sunspots at the feet of the erupting magnetic flux rope associated with the X2.2 flare in AR 11158 on 2011 February 15 exhibit a sudden acceleration of horizontal rotational motion in the photosphere during the flare. The sudden enhancement of negative vorticity in the sunspot areas is co-spatial and co-temporal with the flare, and the region in the vicinity of the polarisation inversion line shows a sudden drop of the horizontal velocity shear after the onset of the flare. They concluded that the horizontal Lorentz force may be the driving force of the abrupt changes of horizontal vortical motions in the photosphere. Analysis of *SDO* data made by Dhara, Ravindra & Banyal (2014) of formation and evolution of 10 solar filaments/prominences in different active regions showed that all events analysed display vortex motions at the filament footpoints in the photosphere during the initial phase of filament eruption, and the sudden onset of a large photospheric vortex motion may destabilize the filament leading to its eruption. Roudier et al. (2018) used the observations of *SDO*, *Global Oscillation Network Group (GONG)*, and *Christian Latouche IMageur Solaire (CLIMSO)* to study filament eruption in AR 12486 triggered by horizontal photospheric flows at the feet of two filaments anchored at supergranular junctions associated with vortical motions. Yan et al. (2018) investigated the occurrence of two successive X-class flares in AR 12673 using *SDO* data. They adopted horizontal vortical flows to study the rotation of three sunspots in this active region and showed that shearing motion and sunspot rotation play a major role in the buildup of free energy and the formation of coronal magnetic flux ropes that produce solar flares and coronal mass ejections.

The aim of this paper is to develop a method of measuring short-term changes and spatiotemporal evolution of structures in network magnetic fields at vertices between supergranules. In particular, we investigate the formation of a magnetic coherent structure via the merger of two plasmoids driven by supergranular vortical flows, using *Hinode* observations in the quiet Sun. We will study the relationship between velocity and magnetic fields during a vortex expansion–contraction interval of a persistent supergranular vortex in the quiet-Sun. In Section 2, we will study the spatiotemporal evolution of an objective (i.e. frame invariant, Haller 2015) supergranular vortex by computing the instantaneous vorticity deviation, and determine the timing of the beginning and the end of the vortex expansion–contraction interval to be studied. In particular, a precise timing of transition from vortex expansion to vortex contraction is identified. In Section 3, we will study the spatiotemporal evolution of the line-of-sight magnetic field, the local current deviation, and the horizontal electromagnetic energy flux in the region of supergranular vertex where the merger of two plasmoids takes place. In Section 4, we will study the formation of a large magnetic coherent structure via plasmoid merging in a vortex expansion–contraction interval by focusing on three topics: (1) transfer of magnetic flux and equipartition of electromagnetic energy flux, (2) incoherent-coherent transition, and (3) disruption of current sheet at the turbulent interface boundary layer. In Section 5, we will present a discussion and conclusions and show that the period of vortex expansion (contraction) exhibits signs of energy buildup (energy dissipation), respectively, typical of relaxation oscillations.

2 VORTEX EXPANSION–CONTRACTION INTERVAL

In this paper, we use the images of the narrow-band filter imager (*NFI*) on-board the *Hinode* satellite, which provides very long and stable time-series of both continuum intensity images and circular polarization maps, ideal for investigating the evolution of network elements and their interaction with vortex flows at supergranular vertices. This *Hinode/NFI* data set has a spatial resolution of 0.32 arcsec per pixel, a cadence of $90s$, and a total field of view of 93 arcsec × 82 arcsec, which was reduced to 69 arcsec × 69 arcsec ($50 \times 50 Mm^2$) to focus on a single supergranular cell (Requerey et al. 2018).

A systematic study was carried out by Chian et al. (2020) for persistent vortices at supergranular junctions at the disc centre of a quiet Sun for a set of ≈22 h continuous high-resolution *Hinode* data, from 08:31:15 UT on 2010 November 2 to 06:19:42 UT on 2010 November 3. A total of 29 long-duration objective vortices were detected for this data set using the technique of Lagrangian coherent structures, with vortex lifetime ranging from 28.5 to 298.3 min (see Fig. 2c in Chian et al. 2020). In particular, a sequence of seven recurrent persistent objective vortices was detected in a region of supergranular vertex (Requerey et al. 2018; Silva et al. 2018; Chian et al. 2019; Giannattasio et al. 2020; Roudier et al. 2021). This network region is dominated by vortical downflows due to strong shears resulting from the interaction of converging flows emanating from a number of adjacent supergranulations (Requerey et al. 2018; Chian et al. 2019). The large spatiotemporal-scale vortices at supergranular junctions observed by *Hinode* are likely the clustering of small spatiotemporal-scale vortices in intergranular lanes (Yadav, Cameron & Solanki 2020, 2021).

Chian et al. (2023) investigated the spatiotemporal dynamics of one vortex from this sequence of supergranular vertex vortices (see vortex B2 in table I of Chian et al. 2020) for a time interval of 30 min, and observed a steady intensification of magnetic field at the interior of the vortex boundary. In this paper, we extend this study to a vortex expansion–contraction interval of 60 min. This supergranular vortex has a lifetime of ≈180 min, from 11:23:49 UT to 14:23:53 UT on 2010 November 2 (frames 115–235). The photospheric horizontal velocity is derived by the local correlation tracking (LCT) method from *Hinode* continuum intensity images with a cadence of 90 s. An objective kinematic vortex is detected by computing the instantaneous vorticity deviation (IVD) along a particle trajectory

$$\mathrm{IVD} := |\omega(\mathbf{x}, t) - \langle \omega(t) \rangle|, \tag{1}$$

which is the integrand of the Lagrangian averaged vorticity deviation (Haller et al. 2016), and $\mathbf{u}$ is the velocity field, the vorticity $\omega = \nabla \times \mathbf{u}$, $\langle \omega(t) \rangle$ is the instantaneous spatial mean of ω in the domain, and $\mathbf{x}$ is the solution of the particle equation of motion $\dot{x} = \mathbf{u}(\mathbf{x}(t), t)$, with $\mathbf{x}(t_0) = \mathbf{x}_0$. An objective vortex centre is given by a local maximum of the IVD field computed on a spatial grid, and the corresponding objective vortex boundary in 2D is given by the outermost closed convex contour line of IVD surrounding the vortex centre.

First, we apply equation (1) to detect this objective vortex in the region of supergranular vertex. Following Chian et al. (2023), we compute the IVD for the vortex expansion–contraction interval by fixing the convexity deficiency parameter (Haller et al. 2016; Silva et al. 2018) to 0.05. Fig. 1(a) shows temporal variations of the vortex area during the entire vortex lifetime, divided sequentially into 4 periods of vortex contraction-expansion–contraction-expansion. The horizontal axis shows the time in terms of data frames, where frame 100 corresponds to 11:01:18 UT on 2010 November 2 and the time between consecutive frames is 90 s. Fig. 1(b) shows the corresponding temporal variations of the total line-of-sight magnetic field at the interior of the objective vortex boundary, divided sequentially into 4 periods of decrease-increase-decrease-increase of the total line-of-sight unsigned magnetic flux. For the remainder of this paper, we will focus on the vortex expansion–contraction interval of 60 min indicated by the horizontal bar in Fig. 1(a), from 12:53:51 UT to 13:53:51 UT on 2010 November 2 (frame 175 to 215). Within this time interval, the transition from vortex expansion to vortex contraction occurs at 13:31:21 UT on 2010 November 2 (frame 200) marked by the vertical dashed line in Fig. 1.

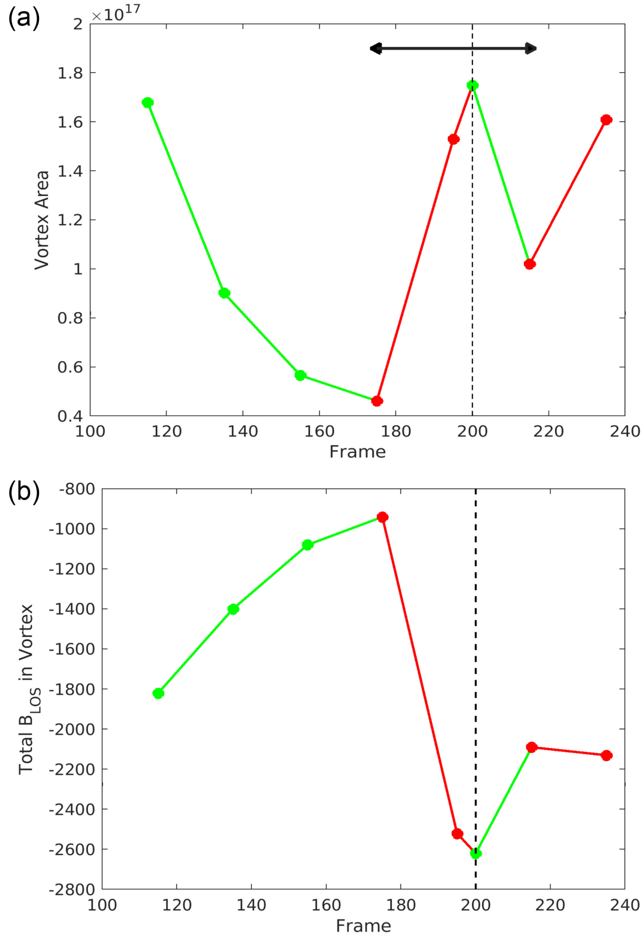

Figure 1. An overview of temporal variations of a supergranular vortex during the vortex lifetime from frame 115 to 235 (180 min): (a) the total objective vortex area (in cm^2); (b) the total line-of-sight magnetic field (in G) at the interior of the vortex boundary. The periods of vortex expansion (contraction) are shaded in red (green), respectively. The time interval between two consecutive solid circles is 20 frames (i.e. 30 min). The horizontal bar marks the duration of a vortex expansion–contraction interval from frame 175 to 215 (60 min) to be studied in this paper; the vertical dashed line denotes the time of vortex expansion–contraction transition at frame 200.

The spatiotemporal patterns of the Instantaneous vorticity deviation computed from equation (1) in the region of supergranular vertex during the vortex expansion–contraction interval are depicted in Fig. 2 at the beginning of the period of vortex expansion (frame 175, Fig. 2a), at the time of transition from vortex expansion to vortex contraction (frame 200, Fig. 2b), and at the end of the period of vortex contraction (frame 215, Fig. 2c). Evidently, Fig. 2 shows that strong vortical flows at the interior of vortex boundary are characterized by the localized regions of high values of the instantaneous vorticity deviation. In Fig. 2, the white cross denotes the vortex centre and the grey line denotes the vortex boundary.

Next, we perform a detailed analysis of the entire 60 min duration of the vortex expansion–contraction interval to refine the overview of 180 min vortex lifetime dynamics of Fig. 1. The overview of Fig. 1 is plotted for an interval of 20 frames (i.e. 30 min) between two solid circles, plus an extra solid circle for frame 200 to mark the transition from vortex expansion to vortex contraction. Fig. 3 shows a refined plot of the vortex expansion–contraction interval for the duration indicated by the horizontal bar in Fig. 1(a) with an interval of 4 frames (i.e. 6 min) between two consecutive solid circles, plus extra solid circles for frames 200, 201, and 202 to determine accurately the timing of vortex expansion–contraction transition. We plot in Fig. 3 time variations of the vortex area (Fig. 3a), the total IVD in the vortex (Fig. 3b), and the maximum IVD in the vortex (Fig. 3c). Fig. 3 confirms the results of Fig. 1 that the vortex dynamics in the vortex expansion–contraction interval (frame 175 to 215) can be divided into two periods: (1) period of vortex expansion (37.5 min) from frame 175 to 200, and (2) period of vortex contraction (22.5 min) from frame 200 to 215. Table 1 lists the numerical values of the vortex area, the total IVD in vortex, and the maximum IVD in vortex, respectively, for the last two frames of the period of vortex expansion (frames 199 and 200) and the first two frames of the period of vortex contraction (frames 201 and 202). Table 1 shows that the transition from vortex expansion to vortex contraction *de facto* takes place at frame 200.

3 MAGNETIC FIELD, ELECTRIC CURRENT DENSITY, AND ELECTROMAGNETIC ENERGY FLUX IN A VORTEX EXPANSION–CONTRACTION INTERVAL

The analysis of Section 2 indicates that the 30 min time interval of *Hinode* data studied by Chian et al. (2023), from frame 175 to 195, corresponds to the initial portion of the period of vortex expansion of 37.5 min. In this paper, we will extend the previous study for the entire vortex expansion–contraction interval of 60 min marked by the horizontal bar in Fig. 1(a), till the end of the period of vortex contraction (frame 215).

Fig. 4 displays the spatiotemporal evolution of the line-of-sight magnetic field in the region of supergranular vertex studied by Chian et al. (2023), superposed by the LIC-maps of the horizontal electric current density and the objective vortex boundary computed by the instantaneous vorticity deviation. Since the measurement of B-vector is not available in our data set and the magnetograms that we use here only show the B component along the line of sight, we calculate the horizontal electric current density from *Hinode* observations of the line-of-sight magnetic field by assuming vertically oriented magnetic fields, which is a reasonable hypothesis for the footpoints of magnetic flux tubes rooted at supergranular junctions

$$J_x = \frac{c}{4\pi}\frac{\partial B_z}{\partial y}, \qquad J_y = -\frac{c}{4\pi}\frac{\partial B_z}{\partial x}, \tag{2}$$

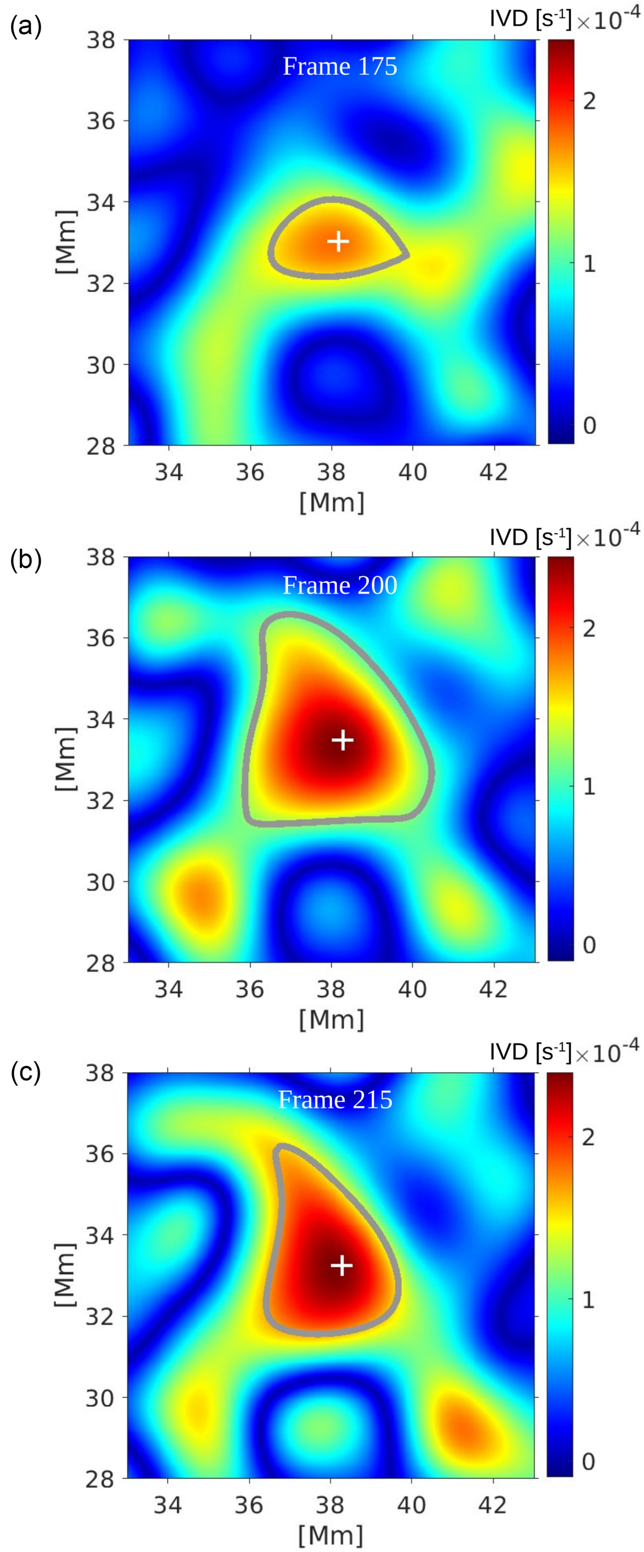

Figure 2. Vortex expansion–contraction interval: instantaneous vorticity deviation, objective vortex boundary, and objective vortex centre of a supergranular vortex: (a) at the beginning of a vortex expansion–contraction interval (frame 175); (b) at the time of vortex expansion–contraction transition (frame 200); (c) at the end of a vortex expansion–contraction interval (frame 215). Grey line denotes the objective vortex boundary and white cross denotes the objective vortex centre given by the maximum of IVD at the interior of the vortex boundary.

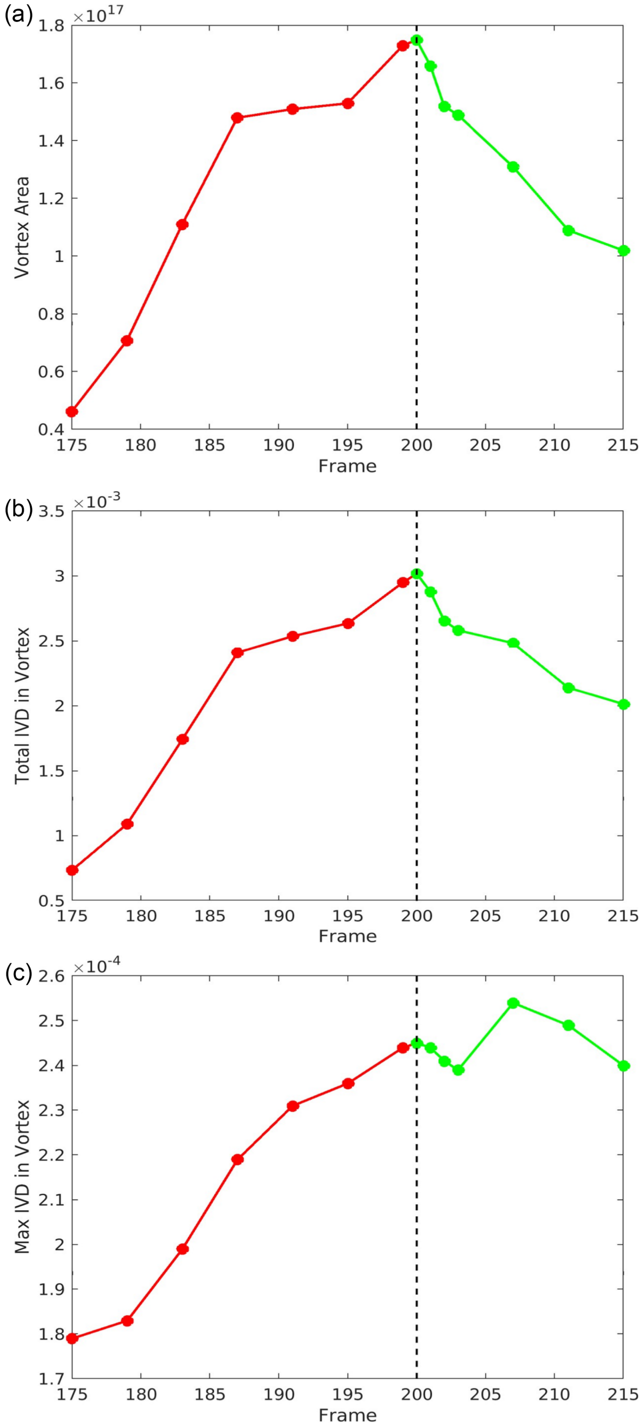

Figure 3. A detailed view of temporal variations during a supergranular vortex expansion–contraction interval from frame 175 to 215: (a) the total objective vortex area (in cm^2); (b) the total instantaneous vorticity deviation (in s^{-1}) at the interior of vortex boundary; (c) the maximum of IVD (in s^{-1}) inside the vortex boundary located at the objective vortex centre. The period of vortex expansion (contraction) during the vortex expansion–contraction interval is shaded in red (green), respectively. The time interval between two consecutive solid circles is 4 frames (i.e. 6 min). The data points for frames 200, 201, and 202 are added to determine precisely the time of transition from vortex expansion to vortex contraction; the vertical dashed line denotes the time of vortex expansion–contraction transition at frame 200.

where B_z is the line-of-sight magnetic field and c is the speed of light. The first two frames (195 and 199) in Fig. 4 belong to the later portion of the period of vortex expansion shown in Fig. 3; whereas the last four frames (203, 207, 211, and 215) belong to the period of vortex contraction. Note that frame 199 is about 90 s before the end of the period of vortex expansion (frame 200), and frame 203 is about 270 s after the beginning of the period of vortex contraction (frame 200). The two arrows denote two plasmoids (magnetic flux tubes) undergoing the merging process at the interior of the vortex boundary. The magenta square denotes the location of the maximum of the line-of-sight magnetic field in the domain, corresponding to the centre of plasmoid-1. It follows from Fig. 4(f) that at the end of the vortex expansion–contraction interval, the plasmoid merging leads to the formation of a stretched magnetic coherent structure associated with strong magnetic fields of the order of a kiloGauss. Note from Fig. 4 that solar plasma turbulence is composed of a multitude of interacting multiscale magnetic flux tubes.

Following Chian et al. (2019)), the two merging plasmoids are identified by a visual inspection of the two interacting closed loops (magnetic islands) of the LIC-maps of the horizontal electric current density computed from the line-of-sight magnetic field inside the vortex boundary, as shown in the background of Fig. 4. The centre of each plasmoid is given by the site of the local maximum of the line-of-sight magnetic field. The centre of plasmoid-1 corresponds to the site of the maximum of the line-of-sight magnetic field in the domain of the merging plasmoids marked by the magenta square in Figs 4.

Fig. 5 exhibits the spatiotemporal evolution of the local current deviation (LCD; Rempel et al. 2017) in the same region of Fig. 4, superposed by the LIC-maps of the horizontal electric current density and the objective vortex boundary. The orange square denotes the location of the maximum of LCD in the domain. Intense current sheets in the merging plasmoids are characterized by the localized regions of high values of LCD. The LCD is given by

$$\mathrm{LCD}(\mathbf{x}, t_0) := |\mathbf{J}(\mathbf{x}, t_0) - \langle \mathbf{J}(t_0) \rangle|. \quad (3)$$

Equation (3) is the integrand of the integrated averaged current deviation introduced by Rempel et al. (2017, 2019) to provide an objective quantification of electric current density. We will show later that the thin current sheet at the interface of two merging plasmoids is unstable and subject to disruption during merging. It follows from Fig. 5(f) that at the end of the vortex expansion–contraction interval, the plasmoid merging leads to the formation of an elongated electric current coherent structure bounded by a shell of intense current sheets.

Recently, numerical simulations of a quiet-Sun by Silva et al. (2022) found that the total electromagnetic energy flux in the photosphere occurs mainly parallel to the photosphere, concentrating in small regions along the intergranular lanes. Thus, it is possible to define a proxy for the horizontal electromagnetic energy flux based only on the horizontal velocities of the small-scale magnetic elements and their longitudinal magnetic flux. Fig. 6 shows the spatiotemporal evolution of the horizontal electromagnetic energy flux in the same regions of Figs 4 and 5, superposed by the LIC-maps of the horizontal velocity and the objective vortex boundary. The horizontal electromagnetic energy flux (Silva et al. 2022)

$$S = \frac{1}{4\pi} u_h B_z^2, \quad (4)$$

is derived from the Poynting vector S in MHD approximation

$$S = \frac{1}{4\pi} \mathbf{B} \times (\mathbf{u} \times \mathbf{B}), \quad (5)$$

Table 1. The vortex area (in cm^2), the total IVD in vortex (in s^{-1}), and the maximum IVD in vortex (in s^{-1}) at the later portion of the period of vortex expansion (frames 199 and 200) and at the earlier portion of the period of vortex contraction (frames 201 and 202) on 2010 November 2 in a supergranular vertex region of the quiet Sun. This table indicates that frame 200 is the timing of vortex expansion–contraction transition.

Frame number	199	200	201	202
Vortex area	1.73×10^{17}	1.75×10^{17}	1.66×10^{17}	1.52×10^{17}
Total IVD in vortex	0.00295	0.00302	0.00288	0.00266
Max IVD in vortex	0.000244	0.000245	0.000244	0.000241

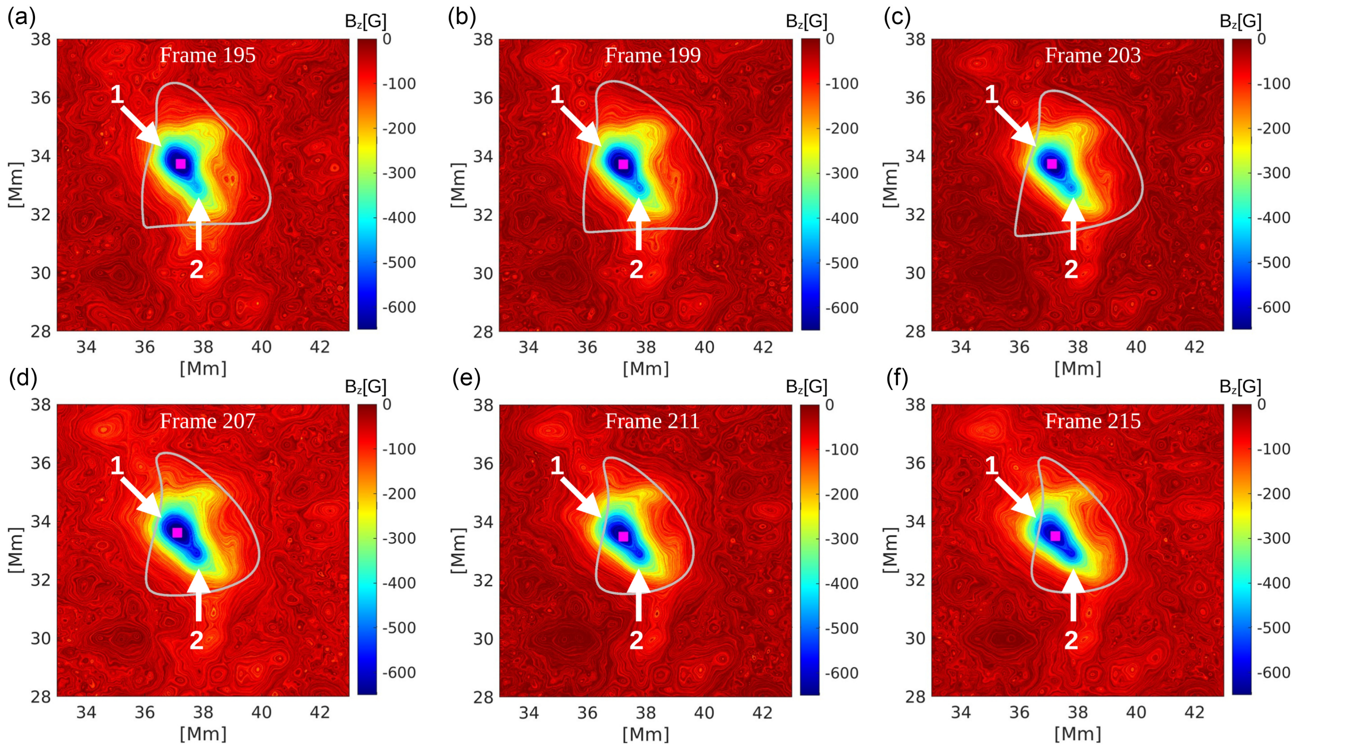

Figure 4. Spatiotemporal dynamics of the line-of-sight magnetic field superposed by LIC-maps of the horizontal electric current density at a supergranular vertex from frame 195 to 215, with an interval of 6 min between two consecutive images. The grey lines denote the objective vortex boundary; the arrows denote the merging plasmoids 1 and 2; the magenta squares denote the locations of the maxima of the line-of-sight magnetic field in the domain located at the centre of plasmoid-1.

where u_h is the modulus of the horizontal velocity, and B_z is the line-of-sight magnetic field. Fig. 6(b) shows that towards the end of the period of vortex expansion (frame 199), the horizontal electromagnetic energy flux of merging plasmoids located adjacent to the centre of vortical flows is fully trapped at the interior of vortex boundary. It follows from Fig. 6(f) that at the end of the vortex expansion–contraction interval, the plasmoid merging leads to the formation of an elongated electromagnetic coherent structure associated with a strong concentration of electromagnetic energy flux.

4 FORMATION OF MAGNETIC COHERENT STRUCTURE VIA PLASMOID MERGING IN A VORTEX EXPANSION–CONTRACTION INTERVAL

In Section 3, we presented a qualitative view of the spatiotemporal evolution of the formation of an elongated magnetic coherent structure in the region of supergranular vertex. In this section, we will present a quantitative analysis of the physical mechanisms leading to this formation. Fig. 7 shows from top to bottom, the temporal variability of the total signed line-of-sight magnetic field at the interior of vortex boundary, the maximum of the local current deviation in the domain of plasmoid merging, the unsigned line-of-sight magnetic field and electromagnetic energy flux at the centre of two merging plasmoids during the entire vortex expansion–contraction interval, from frame 175 to 215. The data set in Fig. 7 is a union of the data from the initial portion of the period of vortex expansion (frame 175–199) studied by Chian et al. (2023) plus the data from this paper (frame 199–215) shown in Figs 4–6. It follows from Fig. 7 that towards the end of the vortex expansion–contraction interval, the modulus of the line-of-sight magnetic field at the centres of plamoid-1 and plasmoid-2 approach each other; furthermore, an equipartition of the modulus of the horizonal electromagnetic energy flux at the centres of plasmoid-1 and plasmoid-2 is reached. Hence, Figs 3 and 7 provide the complete set of quantitative information on the temporal evolution of velocity and magnetic fields in plasmoid merging driven by a persistent supergranular vortex that leads to

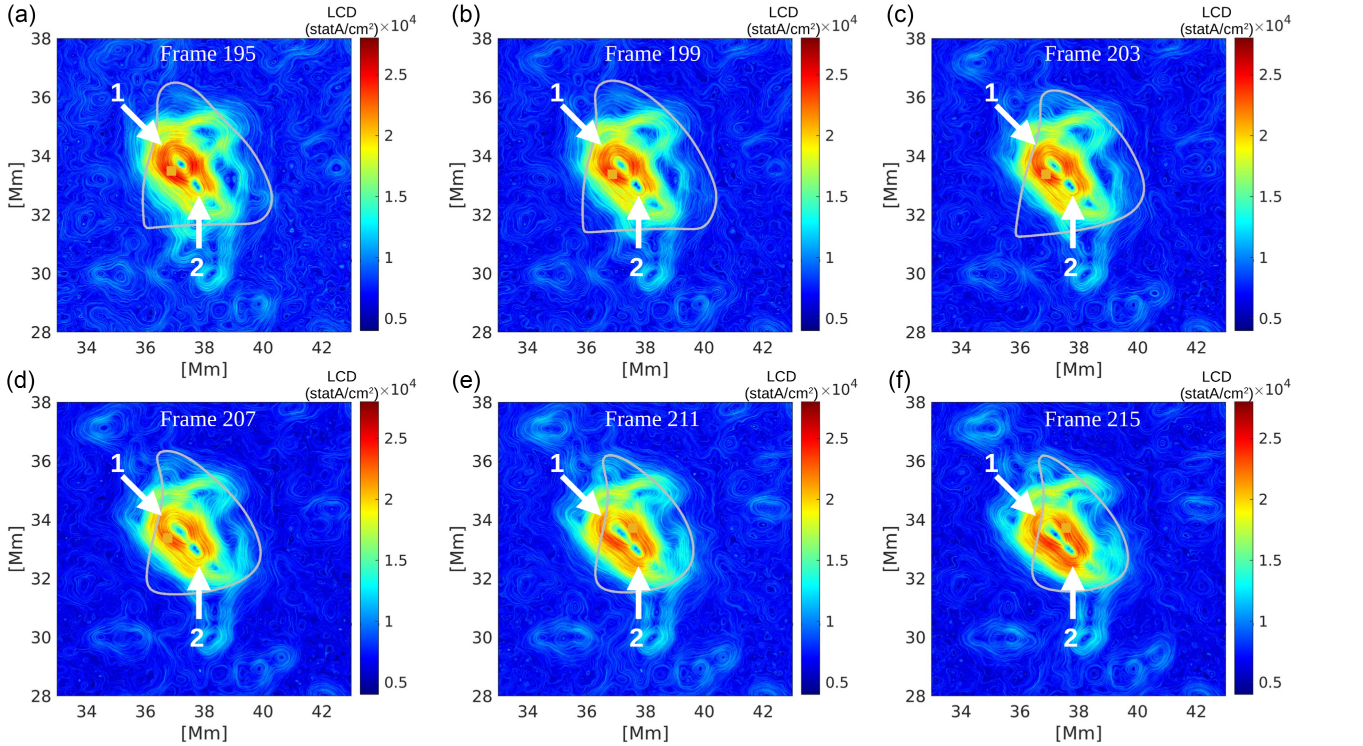

Figure 5. Spatiotemporal dynamics of the LCD superposed by LIC-maps of the horizontal electric current density from frame 195 to 215. The grey lines denote the objective vortex boundary; the arrows denote the merging plasmoids 1 and 2; the orange squares denote the locations of the maxima of LCD over the domain.

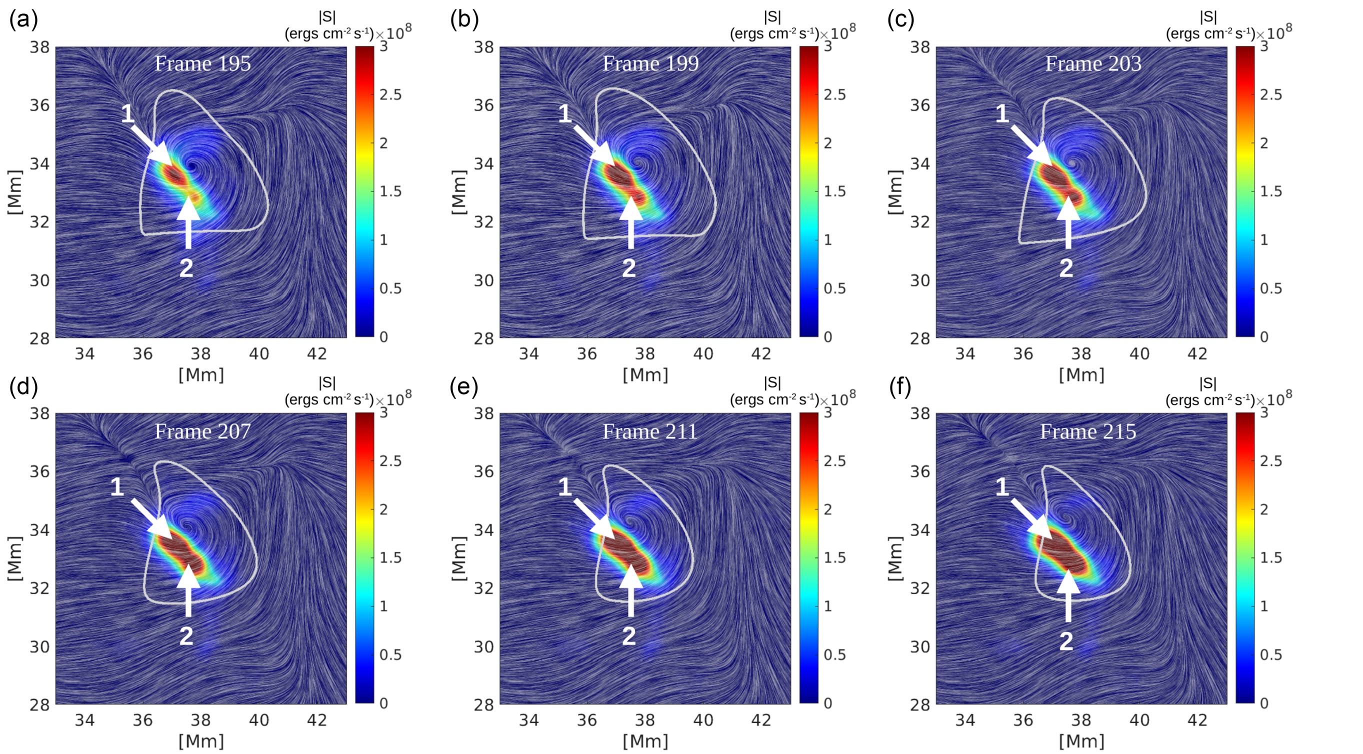

Figure 6. Spatiotemporal dynamics of the horizontal electromagnetic energy flux superposed by LIC-maps of the horizontal photospheric velocity fields from frame 195 to 215. The grey lines denote the objective vortex boundary; the arrows denote the merging plasmoids 1 and 2.

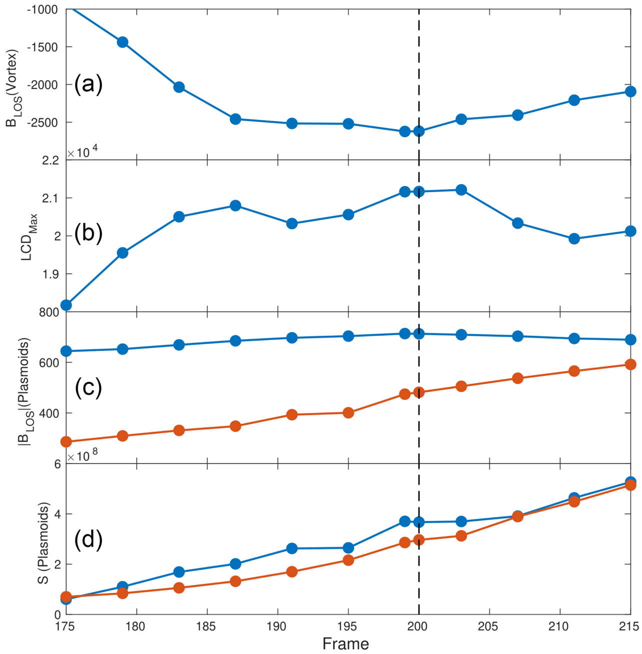

Figure 7. A detailed view of temporal variations in the supergranular vortex expansion–contraction interval (frame 175–215) at the supergranular region of Figs 4–6: (a) the total line-of-sight magnetic field (in G) at the interior of vortex boundary;(b) the maximum of the local current deviation (in statA/cm^2) in the domain of plasmoid merging; (c) the modulus of line-of-sight magnetic field (in G) at the centre of plasmoid-1 (blue) and plasmoid-2 (red), respectively; (d) the modulus of the horizontal electromagnetic energy flux (in ergs cm^{-2} s^{-1}) at the centre of plasmoid-1 (blue) and plasmoid-2 (red), respectively. During the period of vortex expansion, the line-of-sight magnetic field at the centres of plasmoids 1 and 2 shows a steady increase; whereas during the period of vortex contraction, the line-of-sight magnetic field at the centre of plasmoid-1 (2) shows a steady decrease (increase), respectively, indicating a steady transfer of magnetic flux from plasmoid-1 to plasmoid-2. Towards the end of the vortex expansion–contraction interval, the horizontal electromagnetic energy fluxes at the centres of the merging plasmoids 1 and 2 reach similar values that is an indicative of the formation of a large electromagnetic coherent structure. The vertical dashed line denotes the time of vortex expansion–contraction transition at frame 200.

the formation of a large magnetic coherent structure during a vortex expansion–contraction interval of 60 min.

4.1 Transfer of magnetic flux and equipartition of electromagnetic energy flux

Fig. 7(a) shows temporal variations of the total line-of-sight magnetic field at the interior of the vortex boundary during the vortex expansion–contraction interval (frame 175–215). It shows that the modulus of the total line-of-sight magnetic field within the vortex boundary increases continuously during the period of vortex expansion (frame 175–200), and decreases continuously during the period of vortex contraction (frame 200–215). This is consistent with the temporal evolution of vortex area, the total IVD in vortex, and the maximum IVD in vortex seen in Fig. 3 and Table 1. In particular, it confirms that the transition from vortex expansion to vortex contractions occurs at frame 200.

Fig. 7(b) shows temporal variations of the maximum of the local current deviation at the boundary layers of the merging plasmoids during the vortex expansion–contraction interval. On average, the temporal evolution of LCD_{Max} follows the behaviour of the vortex expansion–contraction interval of Figs 3 and 7(a), namely, it increases during the period of vortex expansion and decreases during the period of vortex contraction. The time interval of electric current density decline is indicative of energy dissipation. Note that there are two intervals of LCD_{Max} decline. The first short interval is from frame 187 to 191, and the second longer interval is from frame 203 to 211. The onset of the first interval is co-temporal with a sudden change in the temporal dynamics of vortex area and the total instantaneous vorticity deviation in vortex seen in Figs. 3(a)–(b) whereby their rate of growth slows down considerably from frame 187 onwards, which may lead to the decline of electric current density. The onset (frame 203) of the second interval is co-temporal with the abrupt changes of vorticity seen in Fig. 3, whereby the maximum of the instantaneous vorticity deviation inside the vortex boundary begins a brief interval of rise (frame 203–207) as shown in Fig. 3(c) reaching its peak value of the vortex expansion–contraction interval at frame 207. The measures of maxima such as the maximum IVD in vortex in Fig. 3(c), the maxima of the line-of-sight magnetic field in the region of plasma merging (corresponding to the centre of plasmoid-1) in Fig. 4, and the LCD_{Max} at the electric current density boundary layers in Fig. 7(b) are capable of capturing some subtle details of complex plasma dynamics not shown by other integrated measures.

Fig. 7(c) shows that during the period of vortex expansion (frame 175–200), the modulus of the line-of-sight magnetic field at the centres of both plasmoid-1 and plasmoid-2 increases continuously. However, during the period of vortex contraction (frame 200–215) the modulus of the line-of-sight magnetic field at the centre of plasmoid-1 (plasmoid-2) decreases (increases) continuously. At the time of vortex expansion–contraction transition (frame 200), the modulus of the line-of-sight magnetic field at the centre of plasmoid-1 is considerably higher than the modulus of the line-of sight magnetic field at the centre of plasmoid-2. At the later portion of the period of vortex contraction, the line-of-sight magnetic field at the centre of plasmoid-1 and plasmoid-2 approach each other. This indicates that there is a continuous transfer of magnetic flux from plasmoid-1 to plasmoid-2 during the period of vortex contraction. For the sake of clarity, the numerical values of the modulus of the line-of-sight magnetic field at the centre of the two merging plasmoids during the period of vortex contraction are given in Table 2. Note that weak magnetic flux patches continuously coming from the interior of the supergranular cell and depositing their magnetic fluxes in the network regions. Hence, in addition to the interaction between plasmoids 1 and 2, these two plasmoids also interact with the surrounding regions and can get a certain amount of flux from interacting with the surrounding magnetic patches.

Fig. 7(d) shows that the modulus of the horizontal electromagnetic energy flux at the centre of both plasmoid-1 and plasmoid-2 increases continuously during the vortex expansion–contraction interval. At the time of vortex expansion–contraction transition (frame 200), the electromagnetic energy flux at the centre of plasmoid-1 is much higher than the electromagnetic energy flux at the centre of plasmoid-2. Near the end (frames 207, 211, and 215) of the vortex expansion–contraction interval, an equipartition of the horizontal electromagnetic energy flux at the centre of two merging plasmoids is reached. For the sake of clarity, the numerical values of the modulus of the horizontal electromagnetic energy flux at the centre of plasmoid-1 and plasmoid-2 during the period of vortex contraction are given in Table 2. The onset of equipartition of electromagnetic energy flux in the two merging plasmoids at frame 207 is co-temporal

Table 2. Temporal evolution of the modulus of line-of-sight magnetic field (in G) and the modulus of the horizontal electromagnetic energy flux (in ergs cm^{-2} s^{-1}) at the centre of two merging plasmoids during the period of vortex contraction (frame 200–215) in the supergranular vertex region of the quiet Sun on 2010 November 2.

Frame number	200	203	207	211	215
$\lvert B_{LOS} \rvert$ (plasmoid-1)	713	709	703	694	690
$\lvert B_{LOS} \rvert$ (plasmoid-2)	482	505	537	566	592
S (plasmoid-1)	3.67×10^8	3.70×10^8	3.91×10^8	4.63×10^8	5.27×10^8
S (plasmoid-2)	2.96×10^8	3.13×10^8	3.89×10^8	4.48×10^8	5.14×10^8

with the peak value of the maximum IVD in the vortex as seen in Figs 3(c) and 7(d) and Table 2.

4.2 Incoherent–coherent transition

Fig. 8 gives an overview of the formation of a large magnetic coherent structure at the beginning (frame 175, first column) of the vortex expansion–contraction interval, at the time of vortex expansion–contraction transition (frame 200, second column), and at the end of the vortex expansion–contraction interval (frame 215, third column), respectively. The first, second, and third row of Fig. 8 show the spatiotemporal evolution of the line-of-sight magnetic field, the local current deviation, and the horizontal electromagnetic energy flux, respectively.

At the beginning of the vortex expansion–contraction interval (Fig. 8a), the spatial distribution of magnetic flux in the region of supergranular vertex is inhomogeneous and only a small fraction of the intense magnetic flux concentration is trapped at the interior of vortex boundary. At the time of vortex expansion–contraction transition (Fig. 8d), the entire concentration of intense magnetic flux is trapped within the vortex boundary. At the end of the vortex expansion–contraction interval (Fig. 8g), an elongated magnetic coherent structure is formed showing a homogeneous distribution of magnetic flux.

At the beginning of the vortex expansion–contraction interval (Fig. 8b), intense electric current densities are only seen at the oval closed border encircling plasmoid-1. At the time of vortex expansion–contraction transition (Fig. 8e), the stretching of intense electric current densities begins to encircle the joint border of two merging plasmoids. At the end of the vortex expansion–contraction interval (Fig. 8h), an elongated electric current coherent structure is formed surrounded by a shell of intense current sheet.

At the beginning of the vortex expansion–contraction interval (Fig. 8c), the spatial pattern of the horizontal electromagnetic energy flux is irregular, consisting of fragmented patches of Poynting flux, and only a fraction of the horizontal electromagnetic energy flux is trapped inside the vortex boundary. At the time of vortex expansion–contraction transition (Fig. 8f), the merger of two plasmoids leads to an elongated electromagnetic structure fully trapped at the interior of vortex boundary. At the end of the vortex expansion–contraction interval (Fig. 8i), an elongated coherent structure is formed showing a homogeneous spatial distribution of the horizontal electromagnetic energy flux.

Evidently, Fig. 8 shows that the spatiotemporal evolution of magnetic flux, electric current density, and electromagnetic energy flux demonstrates the complex systems characteristics of incoherent-coherent transition, transforming from the incoherent regime seen at the beginning of vortex expansion–contraction interval seen in Figs 8(a)–(c) to the coherent regime seen at the transition of vortex expansion–contraction seen in Figs 8(d)–(f).

4.3 Disruption of current sheet at the turbulent interface boundary layer

The dynamics of the turbulent boundary layer at the interface of two merging plasmoids is key to the formation of the large magnetic coherent structure, since the thin current sheet at the interface is unstable to plasmoid merging. The disruption (breakup) of current sheets and formation of secondary plasmoids (magnetic islands/flux ropes) are generic features of magnetic reconnection (Loureiro, Schekochihin & Cowley 2007). Secondary plasmoids have been observed in the Earth's magnetotail (Zong et al. 2004) and solar flares (Takasao et al. 2012). Particle-in-cell simulations of Drake et al. (2006) demonstrated that energetic electrons can be accelerated through their interactions with multiple plasmoids in magnetic reconnection. Comisso & Grasso (2016) studied how the plasmoid instability in a Sweet–Parker type current sheet enables fast magnetic reconnection in visco-resistive plasmas.

Huang, Comisso & Bhattacharjee (2017) carried out 2D MHD simulations of two merging magnetic islands to investigate the onset of plasmoid instability by taking into account the evolution process of the current sheet. They found that the amplitude of fluctuations begins to increase when the linear growth rate exceeds advection loss and overcomes the stretching effect of the outflows. The linear growth rate keeps rising until the sizes of plasmoids approach the sizes of the inner layer width of the tearing mode. This leads to the current sheet disruption and the onset of non-linear regime of plasmoid instability. The growth rate then starts to decrease but the reconnection rate begins to increase rapidly, indicating that the disruption of current sheet triggers the onset of fast magnetic reconnection.

Beg, Russell & Hornig (2022) performed 3D MHD simulations of two merging magnetic flux ropes to investigate the relationships between magnetic reconnection and turbulence. The temporal evolution of their simulations can be divided into three phases. A laminar phase starts with Sweet–Parker reconnection onset, followed by non-linear tearing with excitation of secondary plasmoids. A transition phase involving kink instability of central flux rope and turbulent reconnection onset; after the breakdown of central flux rope, the reconnecting layer becomes almost fully stochastic. The final phase begins with ejection of the remnant of central flux rope, which becomes later fully absorbed at outflows, leading to the onset of self-sustaining turbulent reconnection. Two scales in the reconnection layer are identified: an inner scale related to electric current and kinematic vorticity densities, turbulent fluctuations, and outflow jets, and an outer scale linked to field line stochasticity.

MHD numerical simulations of Huang et al. (2017) and Beg et al. (2022) provide in-depth insights for understanding *Hinode* observations of plasmoid merging and its relation to current sheet disruption. An enlarged view of the turbulent interface boundary layer of two merging plasmoids is given in Fig. 9. Fig. 9(a) shows that at the beginning of the vortex expansion–contraction interval, the thin current sheet connecting two merging plasmoids appears stable.

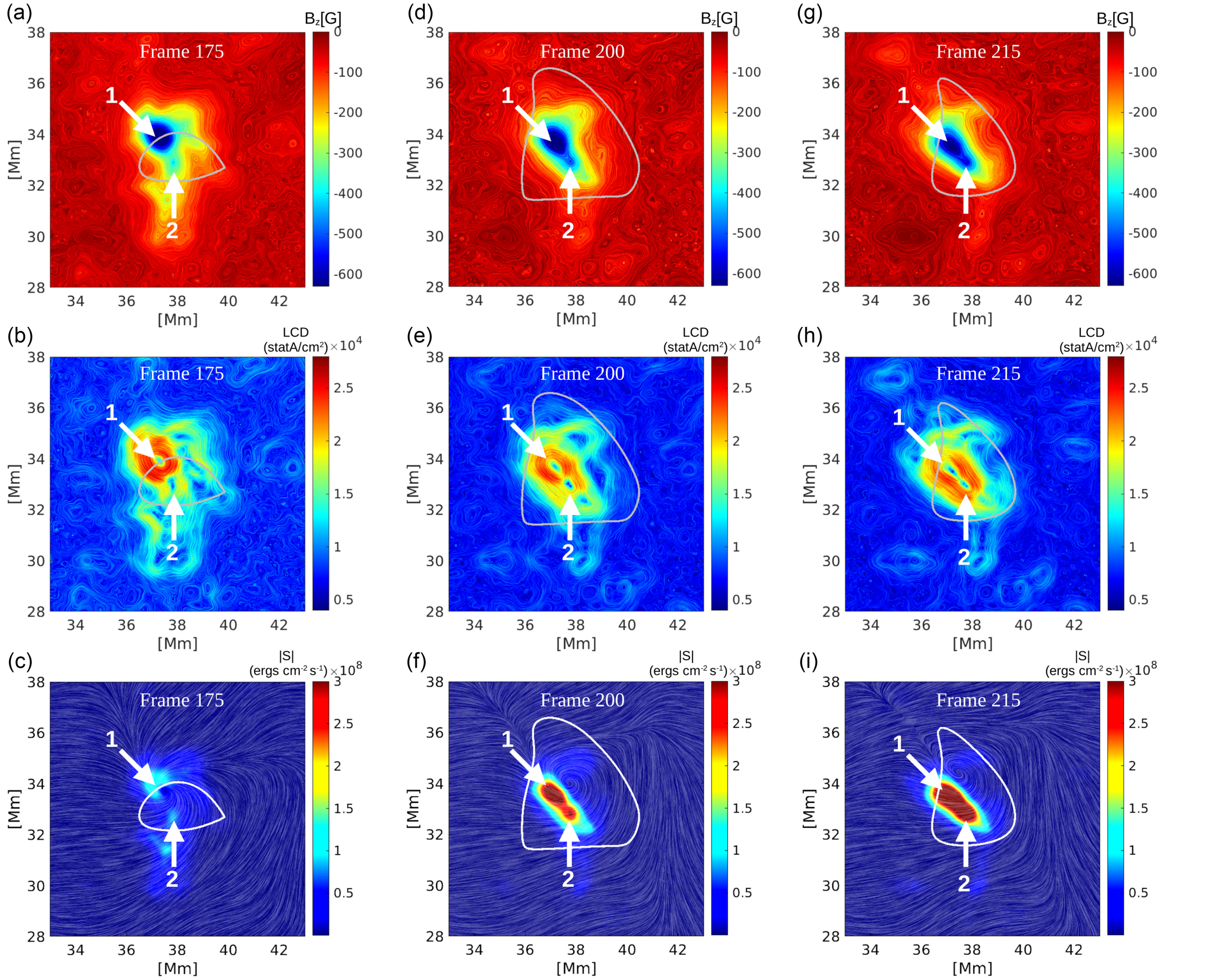

Figure 8. An overview of the formation of a large magnetic coherent structure via plasmoid merging in a vortex expansion–contraction interval (frame 175–215) at the supergranular region of Figs 4–6. The spatiotemporal dynamics of the line-of-sight magnetic field superposed by LIC-maps of the horizontal electric current density (first row), the local current deviation superposed by LIC-maps of the horizontal electric current density (second row), and the horizontal electromagnetic energy flux superposed by LIC-maps of the horizontal photospheric velocity fields (third row) at the beginning of the vortex expansion–contraction interval (frame 175, left column), at the time of the vortex expansion–contraction transition (frame 200, middle column), and at the end of the vortex expansion–contraction interval (frame 215, right column). The vortex expansion allows the transition from an incoherent spatial distribution of electromagnetic energy flux at the beginning of the period of vortex expansion (c) to the an elongated electromagnetic coherent structure at the end of the period of vortex expansion (f).

Fig. 9(b) shows that at the transition of vortex expansion–contraction, the thin current sheet becomes unstable exhibiting signs of disruption. Fig. 9(c) shows that at the end of the vortex expansion–contraction interval, the thin current sheet becomes strongly perturbed, which facilitates the merger of two plasmoids leading to the formation of a large magnetic coherent structure.

A complete view of the spatiotemporal evolution of the turbulent interface boundary layer during the vortex expansion–contraction interval can be obtained by combining fig. 4 of Chian et al. (2023) (frame 175–195) and Fig. 5 of this paper (frame 195–215). An enlarged view of fig. 4(e) of Chian et al. (2023) (see fig. 5 of cited reference) shows that the interface current sheet disruption can already be observed at frame 187, namely, 18 min after the onset of the vortex expansion–contraction interval and 42 min before the end of 60 min vortex expansion–contraction interval. Hence, the disruption of current sheet at the turbulent interface boundary layer plays a central role in the formation of the large magnetic coherent structure during the vortex expansion–contraction interval because the breakup of interface current sheet opens up channels for the transfer of magnetic flux and electromagnetic energy flux between two merging plasmoids, as seen in Fig. 7 and Table 2.

During the early portion of the period of vortex expansion when the interface current sheet is weakly perturbed, the maximum of the local current deviation in the domain of the merging plasmoids is located in the vicinity of the thin interface current sheet connecting two merging plasmoids, as seen in figs 4 and 5 of Chian et al. (2023). However, near the end of the period of vortex expansion and during the period of vortex contraction when the interface current sheet is strongly perturbed, the LCD_{Max} is shifted away from the interface boundary layers to the outer boundary layers encircling the merging plasmoids, as seen in Fig. 5 of this paper. Note that the shifting of the location of the LCD_{Max} from the left (frames 195, 199, 203, 207)

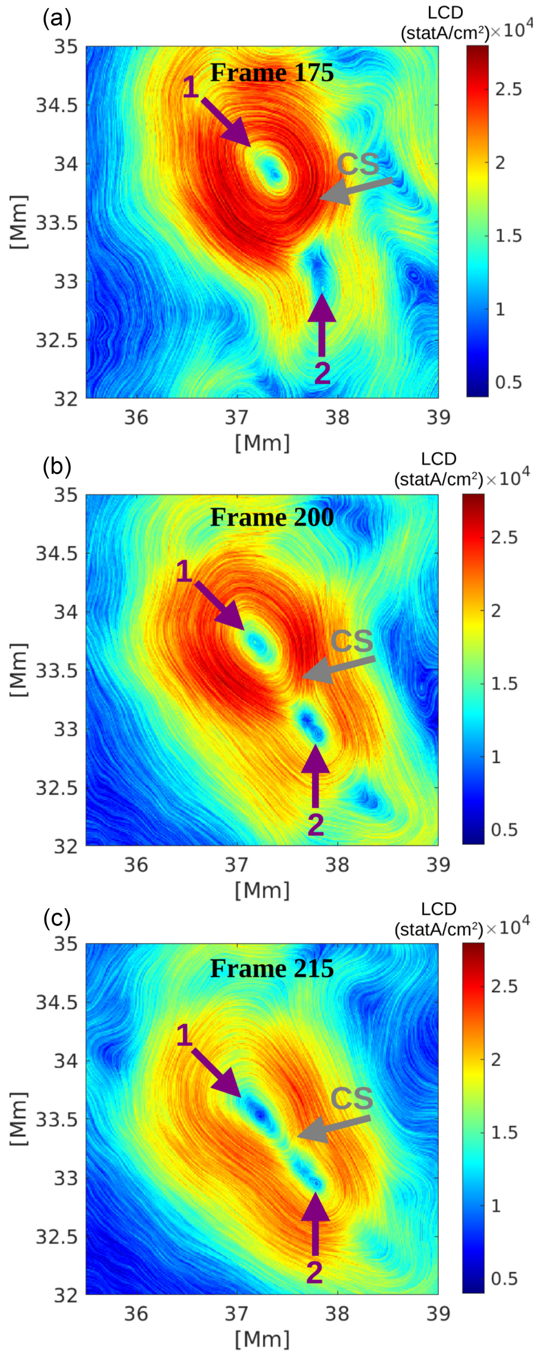

Figure 9. Disruption of a thin current sheet at the turbulent interface boundary layers of two merging plasmoids. Enlarged views of the local current deviation superposed by LIC-maps of the horizontal electric current density of Figs 8(b), (e), and (h), respectively, at the beginning at frame 175 (a) and at the end at frame 215 (c) of the vortex expansion–contraction interval, and at the transition of vortex expansion–contraction at frame 200 (b). The grey arrow marks the location of the disrupting thin current sheet (CS) at the interface of two merging plasmoids; the magenta arrows denote two merging plasmoids. At the beginning of vortex expansion–contraction interval, the interface current sheet appears stable (a). During the period of vortex expansion, the interface current sheet becomes unstable showing the signature of disruption (b). At the end of vortex expansion–contraction interval, the interface current sheet appears strongly disrupted (c).

to the right (frames 211, 215) outer boundary layers seen in of Fig. 5 occurs following the onset of equipartition of electromagnetic energy flux in the merging plasmoids and the peaking of the maximum IVD in vortex seen in Figs 3(c) and 7(d) and Table 2.

5 DISCUSSION AND CONCLUSIONS

Supergranulations are generated by thermal magnetoconvection processes such as magnetized Rayleigh–Bénard convection (Rincon & Rieutord 2018). The radially outward diverging plasma flows originating from the centre of a supergranular cell travel preferentially along the stable manifolds, until they intersect the unstable manifolds at the fixed points of Lagrangian chaotic saddles in supergranular turbulence (Chian et al. 2020, 2023). Note that some of the crossings of stable and unstable manifolds are at saddle points, but most of them are homoclinic and heteroclinic points, not saddle points. Time-dependent Lagrangian boundaries of supergranular cells are given by the unstable manifolds, which serve as sinks for the downdraft of plasma flows that allow the formation of recurrent persistent vortices at supergranular junctions. It is known that the unstable manifolds are co-spatial with the network of intense concentration of magnetic flux at supergranular junctions (Chian et al. 2014, 2019). The stable (unstable) manifolds are given by the ridges of the forward (backward) finite-time Lyapunov exponent, respectively (Haller 2015; Rempel et al. 2023). Our results on the formation of magnetic coherent structure via plasmoid merging driven by supergranular vortical flows contribute to deepen our knowledge of the origin of kiloGauss magnetic flux tubes/ropes related to EUV and X-ray bright points, magnetic tornadoes, and chromospheric/coronal loops in quiet and active Sun.

The velocity and magnetic fields in solar plasma turbulence in the region of supergranular vertex are subject to strong chaotic stretching-twisting-folding resulting from the convergence and interaction of complex flows coming from a number of adjacent supergranular cells, as seen in fig. 1 of Requerey et al. (2018) and fig. 1 of Chian et al. (2019). An objective vortex is typically surrounded by a separatrix formed by stable and unstable manifolds (Haller et al. 2016; Rempel et al. 2017). Vortex expansion/contraction is the consequence of chaotic stretching/shrinking of the stable and unstable manifolds that surround a vortex. Vortex expansion (contraction) is accompanied by vorticity increase (decrease) as confirmed by Fig. 3 and Table 1. Vortex stretching is accompanied by vortex folding to keep the energy of the vortex system constant (Chorin 1994; Kivotides & Leonard 2004).

Elongated magnetic coherent structure during the vortex expansion–contraction interval seen in Figs 4, 5, and 6 is a manifestation of chaotic stretching-shrinking in supergranular turbulence. Elongated granulations have been observed in numerical simulation as well as ground and spacecraft imaging of active and quiet Sun. Elongated granulations in the emerging flux region appear in 3D radiative MHD simulations by Cheung et al. (2008) when quiet-Sun granulations are perturbed by magnetic flux tubes rising into the photosphere through the convection zone, which confirms *Hinode* observation of an ephemeral region during intense flux emergence activity. Lim et al. (2011) use the observation of the *New Solar Telescope (NST)* of the *Big Bear Solar Observatory* and magnetograms from the *Solar Dynamics Observatory/Helioseismic and Magnetic Imager* to demonstrate that elongated granulations, stretching from the penumbral filaments of a sunspot, are photospheric indicators of small-scale flux emergence. Gošić et al. (2021) use observations of *Solar Dynamics Observatory*, *Swedish Solar Telescope*, and *Interface Region Imaging Spectrograph* to follow the evolution of three internetwork magnetic clusters as they emerge into the photosphere at the edges of a supergranular cell and reach the chromosphere and transition region. They found that elongated granules provide the first hint of internetwork flux emerging in the photosphere, and observed elongated magnetic patches in the photosphere and chromosphere concentrating along the intergranular lanes.

Numerical simulations of Kivotides, Mee & Barenghi (2007) conclude that the stretching of magnetic field lines occurs mainly between vortex filaments, resulting from vortex–vortex reconnections in turbulent energy cascade caused by the rate of strain tensor. Hence, it is likely that the elongated magnetic coherent structure seen in Figs 4, 5, and 6 is associated with elongated granulations in the region of supergranular vertex and vortex–vortex reconnections taking place in the intergranular lanes, as suggested by the observations of Gošić et al. (2021) and numerical modelling of Silva et al. (2022). This calls for the need to investigate the relationship between supergranulations and granulations, as well as the impact of velocity gradient associated with the rate of strain tensor in the deformation of magnetic structures.

Vortex boundary acts as a transport barrier that separates turbulent plasmas into two regions: trapped (untrapped) plasmas at the interior (exterior) of vortex boundary, respectively. Chian et al. (2023) showed that at the early portion of the period of vortex expansion, from frame 175 to 195, the modulus of the horizontal electromagnetic energy flux at the centre of two merging plasmoids trapped at the interior of vortex boundary exhibits a steady intensification; whereas the modulus of the horizontal electromagnetic energy flux at the centre of a third plasmoid located at the exterior of vortex boundary exhibits a steady decline (see fig. 8 and Table 2 of the cited reference). The third plasmoid does not show sign of direct interaction with the two merging plasmoids during the vortex expansion–contraction interval studied in this paper, thus plays no role in the flux transfer. By combining the results of this paper and the results of Chian et al. (2023), we obtain a full picture of vortex trapping/untrapping in a vortex expansion–contraction interval.

It follows from figs 1–4 of Chian et al. (2023) and the first two frames (195 and 199) of Figs 4–6 in this paper that during the period of vortex expansion as the vortex area gradually increases, we observe a gradual trapping of the line-of-sight magnetic field, the horizontal electric current density, and the horizontal electromagnetic energy flux of the merging plasmoids. Fig. 8 (middle column) shows that when the vortex area reaches its maximum value at the transition of vortex expansion–contraction (frame 200), we see a complete trapping of the line-of-sight magnetic field, the horizontal electric current density, and the horizontal electromagnetic energy flux of the merging plasmoids. On the other hand, Figs 4, 5, and 6 show that during the period of vortex contraction (frames 203, 207, 211, and 215) as the vortex area gradually decreases, we observe a gradual untrapping of the line-of-sight magnetic field, the horizontal electric current density, and the horizontal electromagnetic energy flux of the merging plasmoids. It follows from Fig. 4 that the untrapping of magnetic flux impacts mostly the outer region of plasmoid-1, whereas plasmoid-2 remains fully trapped. It is worth mentioning that the modulus of the line-of-sight magnetic field at the centre of plasmoid-1 exhibits a steady increase (decrease) during the period of vortex expansion (contraction), respectively, as seen in Fig. 7(c) and Table 2. In contrast, the modulus of the line-of-sight magnetic field at the centre of plasmoid-2 exhibits a steady increase during the entire vortex expansion–contraction interval, intensifying from 286 G to 591 G in 60 min.

The physical mechanisms that contribute to the formation of elongated magnetic coherent structure in the supergranular vortex expansion–contraction interval can be summarized as follows: (1) Turbulent magnetoconvection flows from adjacent supergranulations converge and interact at supergranular junctions, allowing the generation of recurrent long-duration vortices. (2) Incoherent-coherent transition transforms an initially incoherent structure consisted of irregular patterns of magnetic flux and fragmented patches of electromagnetic energy flux at the beginning of the period of vortex expansion (frame 175) into a coherent structure with regular patterns of concentration of magnetic flux and electromagnetic energy flux at the end of the period of vortex expansion (frame 200). (3) During the period of vortex expansion (from frame 175 to 200), the steadily increasing vortex area leads to a complete trapping of magnetic flux, electric current density, and electromagnetic energy flux at the interior of vortex boundary. (4) During the period of vortex contraction (from frame 200 to 215), the steadily decreasing vortex area allows a partial untrapping of magnetic flux, electric current density, and electromagnetic energy flux. (5) The disruption of the thin current sheet at the turbulent interface boundary layer facilitates the transfer of magnetic flux and equipartition of electromagnetic energy flux in the merging plasmoids. (6) The supergranular-granular turbulence energy cascade induced by vortex reconnections leads to the elongation of magnetic flux, electric current density, and electromagnetic energy flux of the magnetic coherent structure encircled by a shell of intense current sheet.

Our detailed analysis of short-term changes of the dynamics and structure of network magnetic fields in a supergranular vortex expansion–contraction interval can be useful for understanding the dynamics and structure of solar cycles, including solar cycles at the Maunder-like minimum when the Sun is possibly associated with ephemeral regions rather than sunspots (Riley et al. 2016). Since granulations and supergranulations are permanent features of solar magnetoconvection, it is likely that magnetic coherent structures such as photospheric plasmoids studied in this paper are ubiquitous features of network magnetic fields even during the Maunder-like minimum with low-level of magnetic activities.

Relaxation oscillations are ubiquitous in nature, e.g. solar cycles in astrophysical systems, cardiovascular cycles in biomedical systems, and business cycles in socio-economic systems. The temporal dynamics of solar cycles, cardiovascular cycles, and business cycles display universal characteristics of chaotic/stochastic intermittency, which can be modelled by the van der Pol equation (van der Pol & van der Mark 1928; Mininni, Gómez & Mindlin 2000; Chian, Rempel & Rogers 2006).

In this paper, our analysis of the spatiotemporal evolution of photospheric turbulence at the footpoints of two interacting magnetic flux tubes at supergranular junctions unravelled some fundamental characteristics of relaxation oscillations in solar and astrophysical magnetism. The observations of *Hinode* in a vortex expansion–contraction interval render support for the chaotic/stochastic nature of solar turbulence evidenced by formation of magnetic coherent structure (Section 4.1), incoherent-coherent transition (Section 4.2), and current sheet disruption (Section 4.3). Solar flares and coronal mass ejections in active regions and microflares and mini-CMEs in quiet regions are the results of recurrent intervals of buildup-dissipation of kinematic and electromagnetic energy. We have shown in Fig. 7(b) that the electric current density in plasmoid merging at the interior of a supergranular vortex shows the features of energy buildup (dissipation) during the period of vortex expansion (contraction), respectively. Since the electric current density is a measure of the degree of twisting/untwisting of magnetic field lines inside a magnetic flux rope (Pontin & Priest 2022; Raphaldini, Prior & MacTaggart 2022), the methodology developed in this paper can be readily applied to improve the prediction of astrophysical flare eruptions (Kusano et al. 2020) and the understanding of the origin of stellar cycles (Martin 2024).

ACKNOWLEDGEMENTS

This paper is dedicated to Dr Phillip Charles Clemmow for his pioneer works on plasma electrodynamics. ACLC is grateful to Dr Clemmow for supervising his PhD studies on relativistic nonlinear waves in plasmas at DAMTP, University of Cambridge. The authors are indebted to the reviewer for valuable comments. ACLC thanks Drs. Alexander Russell, Gunnar Hornig, Raheem Beg, and Karen Meyer for their kind hospitality and stimulating discussion at University of Dundee. The data used here were acquired in the framework of the Hinode Operation Plan 151 'Flux replacement in the solar network and internetwork'. We thank the Hinode Chief Observers for the efforts they made to accommodate our demanding observations. Hinode is a Japanese mission developed and launched by ISAS/JAXA, with NAOJ as a domestic partner and NASA and STFC (UK) as international partners. Financial support by the State Agency for Research of the Spanish Ministerio de Ciencia e Innovación through grant RTI2018-096886-B-C5 (including FEDER funds) and through a Center of Excellence Severo Ochoa award to Instituto de Astrofíísica de Andalucía (SEV-2017-0709) is gratefully acknowledged. MG was supported by NASA contract NNM07AA01C (Solar-B (Hinode) Focal Plane Package Phase E). ELR acknowledges Brazilian agency CNPq (Grant 306920/2020-4) for the financial support.

DATA AVAILABILITY

The data underlying this article will be shared on reasonable request to the corresponding author.

REFERENCES

Bale S. D. et al., 2021, ApJ, 923, 174
Beg R., Russell A. J. B., Hornig G., 2022, ApJ, 940, 94
Chae J., Martin S. F., Yun H. S., Kim J., Lee S., Goode P. R., T S., Wang H., 2001, ApJ, 548, 497
Cheung M. C. M., Schussler M., Tarbell T. D., Title A. M., 2008, ApJ, 687, 1373
Chian A. C.-L., Rempel E. L., Rogers C., 2006, Chaos Solitons Fractals, 29, 1194
Chian A. C.-L., Rempel E. L., Aulanier G., Schmieder B., Shadden S. C., Welsch B. T., Yeates A. R., 2014, ApJ, 786, 51
Chian A. C.-L., Silva S. S. A., Rempel E. L., Gošić M., Kusano L. R. B. R. K., Miranda R. A., Requerey I. S., 2019, MNRAS, 488, 3076
Chian A. C.-L., Silva S. S. A., Rempel E. L., Rubio L. R. B., Gošić M., Kusano K., Park S. H., 2020, Phys. Rev. E, 102, 060201(R)
Chian A. C.-L., Rempel E. L., Silva S. S. A., Rubio L. R. B., Gošić M., 2023, MNRAS, 518, 4930
Chorin A. J., 1994, Phys. Plasmas, 23, 032111
Comisso L., Grasso D., 2016, Phys. Plasmas, 23, 032111
Dhara S. K., Ravindra B., Banyal R. K., 2014, Solar Phys., 289, 4481
Drake J. F., Swisdak M., Che H., Shay M. A., 2006, Nature, 443, 553
Fargette N. et al., 2021, ApJ, 919, 96
Giannattasio F., Consolini G., Berrilli F., Moro D. D., 2020, ApJ, 904, 7
Gold T., Hoyle F., 1960, MNRAS, 120, 89
Gošić M., Rubio L. R. B., Suarez D. O., Katsukawa Y., del Toro Iniesta J. C., 2014, ApJ, 797, 49
Gošić M., Pontieu B. D., Rubio L. R. B., Dalda A. S., Pozuelo S. E., 2021, ApJ, 911, 41
Hagenaar H. J., 2001, ApJ, 555, 448
Hagenaar H. J., Schrijver C. J., Title A. M., 2003, ApJ, 584, 1107
Hagenaar H. J., DeRosa M. L., Schrijver C. J., 2008, ApJ, 678, 541
Haller G., 2015, Annu. Rev. Fluid Mech., 47, 137
Haller G., Hadjighasem A., Huhn M. F. F., 2016, J. Fluid Mech., 795, 136
Harvey K. L., Martin S. F., 1973, Solar Phys., 32, 389
Harvey K. L., Harvey J. W., Martin S. F., 1975, Solar Phys., 40, 87
Huang Y.-M., Comisso L., Bhattacharjee A., 2017, ApJ, 849, 75
Innes D. E., Genetelli A., Attie R., Potts H. E., 2009, A&A, 495, 319
Kivotides D., Leonard A., 2004, Europhys. Lett., 66, 69
Kivotides D., Mee A. J., Barenghi C. F., 2007, New J. Phys., 9, 291
Kusano K., Iju T., Bamba Y., Inoue S., 2020, Science, 369, 587
Leighton R. B., 1964, ApJ, 140, 1547
Leighton R. B., Noyes R. W., Simon G. W., 1962, ApJ, 135, 474
Lim E.-K., Yurchyshyn V., Abramenko V., Ahn K., Cao W., 2011, ApJ, 740, 82
Loureiro N. F., Schekochihin A. A., Cowley S. C., 2007, Phys. Plasmas, 14, 100703
Martin S. F., 1990, in Stenflo J. O., ed., Solar Photosphere: Structure, Convection, and Mangetic Fields. International Astronomical Union, Kluwer Academic Publishers, Dordrecht, p. 129
Martin S. F., 2024, Front. Astron. Space Sci., 10, 1177097
Mininni P. D., Gómez D. O., Mindlin G. B., 2000, Phys. Rev. Lett., 85, 5476
Pontin D. I., Priest E. R., 2022, Living Rev. Solar Phys., 19, 1
Raphaldini B., Prior C. B., MacTaggart D., 2022, ApJ, 927, 156
Rempel E. L., Chian A. C.-L., Beron-Vera F. J., Haller G., Szanyi S., 2017, MNRAS, 466, L108
Rempel E. L., Gomes T. F. P., Silva S. S. A., Chian A. C.-L., 2019, Phys. Rev. E, 99, 043206
Rempel E. L., Chian A. C.-L., Silva S. S. A., Fedun V., Verth G., Miranda R. A., Gošić M., 2023, Rev. Mod. Plasma Phys., 7, 32
Requerey I. S., Cobo B. R., Gošić M., Rubio L. R. B., 2018, A&A, 610, A84
Riley P. et al., 2016, ApJ, 802, 105
Rincon F., Rieutord M., 2018, Living Rev. Solar Phys., 15, 6
Roudier T., Schmieder B., Filippov B., Chandra R., Malherbe J. M., 2018, A&A, 618, A43
Roudier T., Švanda M., Malherbe J. M., Ballot J., Korda D., Frank Z., 2021, A&A, 647, A178
Schrijver C. J., Harvey K. L., 1994, Solar Phys., 150, 1
Silva S. S. A., Rempel E. L., Gomes T. F. P., Requerey I. S., Chian A. C.-L., 2018, ApJ, 863, L2
Silva S. S. A., Murabito M., Jafarzadeh S., Stangliani M., Verth G., Ballai I., Fedun V., 2022, ApJ, 927, 146
Simon G. W., Leighton R. B., 1964, ApJ, 140, 1120
Simon G. W., Title A. M., Weiss N. O., 2001, ApJ, 561, 427
Takasao S., Asai A., Isobe H., Shibata K., 2012, ApJ., 745, L6
Title A., 2000, Phil. Trans. R. Soc. Lon, 358, 657
Tu C.-Y., Zhou C., Marsch E., Xia L.-D., Zhao L., Wang J.-X., Wilhelm K., 2005, Science, 308, 519
van der Pol B., van der Mark J., 1928, Phil. Mag., 6, 763
van Driel-Gesztelyi L., Green L. M., 2015, Living Rev. Solar Phys., 12, 1
Wang S., Liu C., Deng N., Wang H., 2014, ApJ, 782, L31
Yadav N., Cameron R. H., Solanki S. K., 2020, ApJ., 894, L17
Yadav N., Cameron R. H., Solanki S. K., 2021, A&A, 645, A3
Yan X. L., Wang J. C., Pan G. M., Kong D. F., Xue Z. K., Yang L. H., Li Q. L., Feng X. S., 2018, ApJ, 856, 79
Yang B., Jiang Y., Yang J., Hong J., Xu Z., 2015, ApJ, 803, 86
Zhou G., Wang J., Jin J., 2013, Solar Phys., 283, 273
Zong Q.-G. et al., 2004, Geophys. Res. Lett., 31, L18803

This paper has been typeset from a TEX/LATEX file prepared by the author.